How to cite: Angew. Chem. Int. Ed. 2024, e202401373
doi.org/10.1002/anie.202401373

Solid-State Electrolytes | Very Important Paper

A Universal Self-Propagating Synthesis of Aluminum-Based Oxyhalide Solid-State Electrolytes

Simeng Zhang[+], Yang Xu[+], Han Wu, Tianlu Pang, Nian Zhang, Changtai Zhao, Junyi Yue, Jiamin Fu, Shengjie Xia, Xiangzhen Zhu, Guanzhi Wang, Hui Duan, Biwei Xiao, Tao Mei, Jianwen Liang, Xueliang Sun,* and Xiaona Li**

Abstract: Inorganic solid-state electrolytes (SSEs) play a vital role in high-energy all-solid-state batteries (ASSBs). However, the current method of SSE preparation usually involves high-energy mechanical ball milling and/or a high-temperature annealing process, which is not suitable for practical application. Here, a facile strategy is developed to realize the scalable synthesis of cost-effective aluminum-based oxyhalide SSEs, which involves a self-propagating method by the exothermic reaction of the raw materials. This strategy enables the synthesis of various aluminum-based oxyhalide SSEs with tunable components and high ionic conductivities (over 10^{-3} S cm^{-1} at 25 °C) for different cations (Li^+, Na^+, Ag^+). It is elucidated that the amorphous matrix, which mainly consists of various oxidized chloroaluminate species that provide numerous sites for smooth ion migration, is actually the key factor for the achieved high conductivities. Benefit from their easy synthesis, low cost, and low weight, the aluminum-based oxyhalide SSEs synthesized by our approach could further promote practical application of high-energy-density ASSBs.

Introduction

The achievement of solid-state electrolytes (SSEs) with superionic conductivity (up to 10^{-2} S cm^{-1})[1] surpasses liquid electrolytes trailblazing for all-solid-state batteries (ASSBs) with high safety and high-energy densities. Great efforts have been devoted to discovering various types of SSEs and evaluation in terms of conductive property and chemical stability. The promising high ionic conductivities and better compatibility with high-voltage cathode materials of halide-based SSEs compared with classical sulfide-, polymer-based SSEs, has led to a gain in research attention of the former.[2] For example, the research team in Panasonic reported the Li_3YCl_6/Li_3YBr_6 SSEs with room-temperature (RT) ionic conductivity over 10^{-3} S cm^{-1} in 2018[2a] and then further developed oxychloride $LiMOCl_4$ (M = Nb, Ta) SSEs with ultra-high ionic conductivities over 10^{-2} S cm^{-1} in 2023.[1b] Despite the scientific importance, they still face a huge challenge with the energy-consuming synthesis routes, such as the mostly adopted high-energy mechanical ball-milling or high-temperature annealing synthesis.[3] The reaction involved usually occurs in a confined space, for example, the mill pots and the sealed quartz tubes, thus significantly limiting the yield of the final product. Thus, simple, economic, and large-scale synthesis design is the key accelerator for the development and practical application of SSEs.

To overcome these limitations, we go over the chemical reactions involved in the halide SSEs production, which are mostly in the general form: $aLiX + MX_b \rightarrow Li_aMX_{(a+b)}$, or

[*] Dr. S. Zhang,[+] H. Wu, J. Yue, S. Xia, X. Zhu, G. Wang, Prof. X. Sun, Prof. X. Li
Eastern Institute for Advanced Study
Eastern Institute of Technology
Ningbo, Zhejiang 315200, P. R. China
E-mail: xli@eitech.edu.cn
xsun@eitech.edu.cn

Dr. S. Zhang,[+] Y. Xu,[+] Prof. C. Zhao, J. Yue, G. Wang, Prof. B. Xiao, Prof. J. Liang
Solid State Batteries Research Center
GRINM (Guangdong) Institute for Advanced Materials and Technology
Foshan, Guangdong, 528051, P. R. China
E-mail: liangjianwen@grinm.com

Y. Xu,[+] Dr. T. Mei
School of Materials Science and Engineering
Hubei University
Wuhan 430062, P. R. China

T. Pang
National Key Laboratory of Materials for Integrated Circuits,
Shanghai Institute of Microsystem and Information Technology,
Chinese Academy of Sciences
Shanghai 200050. P. R. China

Dr. N. Zhang
Shanghai Synchrotron Radiation Facility, Shanghai Advanced Research Institute
Chinese Academy of Sciences
Shanghai 201204, P. R. China

Dr. J. Fu, Dr. H. Duan
Department of Mechanical and Materials Engineering
University of Western Ontario
London, ON N6A 5B9, Canada

[+] These authors contribute equally to this work.

$Li_2O + MX_a \rightarrow Li_2MOX_a$ (X = halogen elements).[2d,4] Therefore, extra energy (mechanical energy or heat) is usually consumed to promote the chemical reaction. However, if the chemical reactions are exothermic with released energy, they can proceed by themselves. Self-propagating high temperature synthesis is one typical example, which involves compressed reactant powder mixtures ignited to trigger the exothermic reaction. Sometimes, the reaction can even self-initiate at RT, which is highly cost-efficient.[5] In this case, the formation of a target product can be achieved by designing reactions with extremely favorable by-products as driving force.

Regarding this quest, here we report a facile self-propagating route for the synthesis of highly conductive aluminum oxyhalide-based SSEs. The reaction is spontaneous and can occur at low temperature by pressing the hand-mixed raw materials (for example, LiI, $AlCl_3$, and Sb_2O_3) and final aluminum oxyhalide-based SSEs can be obtained after fully removing $SbCl_3$. The synthesis route can be further extended to other monovalent ion conductors with conductivity over 10^{-3} S cm^{-1}, such as Na^+ and Ag^+. More importantly, we proved that it is the amorphous matrix rather than the crystalline phases within the aluminum oxyhalide SSEs that contribute to the fast ion migration. In the course of our research, a study by Hu et al. on the viscoelastic inorganic glass has been published.[6] We acknowledge this work by introducing oxygen into $LiAlCl_4$ to make them with polymer-like viscoelasticity but hope to demonstrate here that it is more efficient to obtain the target SSEs by utilizing the energy released by the exothermic reaction and thus the designed synthesis route is of a much wider applicability.

Results and Discussion

The aluminum oxyhalide-based (AOC-*x*MX, M = Li, Na, Ag, X = Cl, Br, I) SSEs were synthesized from a self-propagating reaction followed by the removal of the by-product and increase the crystallinity. The Density Functional Theory (DFT) calculated reaction enthalpies (ΔH_{rxn}) between different chemicals (such as LiCl, $AlCl_3$) and Sb_2O_3 were compared in Figure 1a. Only the enthalpy of the reaction between $AlCl_3$ and Sb_2O_3 is negative (possible reactions see Equation 1,2).

$$2AlCl_3 + Sb_2O_3 \rightarrow Al_2O_3 + 2SbCl_3 \quad (1)$$

$$3AlCl_3 + Sb_2O_3 \rightarrow 3AlOCl + 2SbCl_3 \quad (2)$$

The ΔH_{rxn} calculated by DFT is -316.641 kJ mol^{-1} and -107.821 kJ mol^{-1}, respectively, corresponding to the formation of Al_2O_3 and AlOCl, demonstrating the exothermic characteristic that releases heat during the reaction. Similar experiments with different molar ratios of $AlCl_3$ and Sb_2O_3 in Figure S1–3 and Supplementary Video 1,2 also proved the heat releasing phenomenon of these reactions. More detailed information about the selection of $AlCl_3$ and Sb_2O_3 by screening reaction enthalpy of oxides and halides is shown in Table S1.

It is supposed that the energy/heat released here can be used to trigger the chemical reaction when involving various salts into the system to obtain the final highly conductive AOC-*x*MX SSEs (Figure 1b, c). The reaction was carried out in an argon-filled glovebox and self-initiated once pressed the hand-mixed reactants. Taking the synthesis of AOC-2LiCl SSE as an example, once mixed the raw materials (LiCl, $AlCl_3$, Sb_2O_3, molar ratio of 2:4.5:1, see text in Supporting Information for further details of the designed molar ratio, Table S2) in an agate mortar and then pressed at ~300 MPa, the pellet will go through a self-propagating reaction. An intense white smoke of volatilized $SbCl_3$ (melting point of 73.4 °C, boiling point of 222.6 °C) by-product is released during the exothermic reaction process. The highest exothermic temperature of the reaction monitored is around 140–165 °C (Figure 1d, S4, Supplementary Video 3,4). Light yellow residual along with colorless solutions can be seen after the self-initiated reaction.

As mentioned above, the highest temperature during the self-propagating reaction can reach up to 162 °C, which is higher than the co-melting point of 143 °C for the $LiAlCl_4$ formation in the LiCl-$AlCl_3$ phase diagram.[7] However, the compositions are complicated with the existence of oxygen in the reaction system. Previous studies on the oxidized molten tetrachloroaluminate salts have demonstrated that there's no free O^{2-} instead of the existence of multiple oxidized chloroaluminate species.[8] Several equilibriums might be achieved in the molten system (Figure 2a). Thus, different types of oxidized chloroaluminate species ($[Al_aO_mCl_n]^{(3a-2m-n)}$, Figure 2b)[8a,9] can be formed from the combination of the above basic ions as presented in. Similarly, it's supposed that there should also be similar $[Al_aO_mCl_n]^{(3a-2m-n)}$ species formed in the colorless solutions during the self-propagating reaction in our case. The colorless solutions of the intermediates were analyzed by Raman spectra (Figure 2c). The Raman spectra of the colorless solution formed after the self-propagating reaction are different from that of $LiAlCl_4$ counterpart. The typical peaks at 100–200 cm^{-1} should be assigned to mixed stretching and bending. The peaks at 315–390 cm^{-1} regions are caused by the stretching of $AlCl_2$ groups, the bending of OAl_2, and the symmetric stretching of Al–Cl bonds.[8b] The results confirmed the formation of $[Al_aO_mCl_n]^{(3a-2m-n)}$ intermediates after the self-propagating reaction. The existence of $SbCl_3$ residual can also be seen in the Raman spectra when detected in different sites of the same sample. Therefore, the products were further heated in specific temperatures to remove $SbCl_3$ by-product totally (see details in Method). Most of the Raman spectra disappear after the further heating process (Figure S5) of the AOC-2LiCl sample.

The X-ray diffraction (XRD) patterns of the final AOC-2LiCl sample are presented in Figure 2d. Weak XRD peaks assigned to LiCl and $LiAlCl_4$ can be seen (red line). X-ray photoelectron spectroscopy (XPS) proves that almost full removal of $SbCl_3$ residual (Figure S6). The XRD patterns of other AOC-*x*LiCl samples synthesized from different molar ratios (*x*: 4.5: 1 for LiCl, $AlCl_3$, and Sb_2O_3) were also

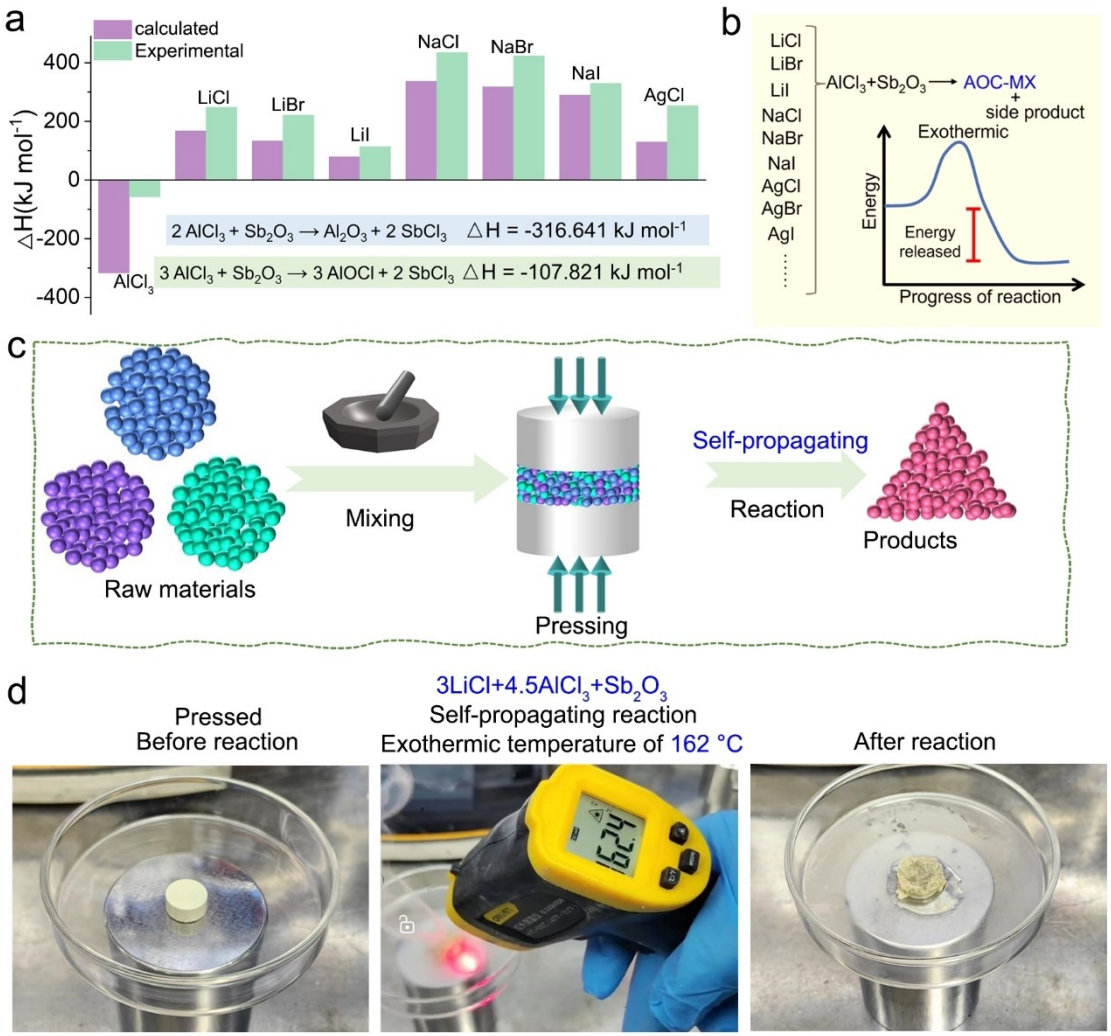

Figure 1. (a) The calculation of reaction enthalpies between different chemicals and Sb_2O_3. Insert is the reaction enthalpies of the possible reaction between $AlCl_3$ and Sb_2O_3. See Supporting Information for further details. (b) The illustration of using the energy released by the exothermic reaction between $AlCl_3$ and Sb_2O_3 to trigger the chemical reaction when involving various salts to obtain the final aluminum oxychloride-based (AOC-MX) SSEs. (c) The schematical illustration of the self-propagating reaction. (d) The self-propagating reaction process of the mixture of LiCl, $AlCl_3$, and Sb_2O_3.

compared in Figure 2d. When $x=1$, the XRD patterns can be assigned to $LiAlCl_4$ and AlOCl. When $x\geq 3$, obvious peaks of LiCl can be detected, especially for the sample with $x=6$. Corresponding Arrhenius plots of the AOC-xLiCl samples with different molar ratios were displayed in Figure 2e. The room-temperature (RT) ionic conductivities are 2.69×10^{-5}, 1.24×10^{-3}, 2.75×10^{-4}, and 3.05×10^{-4} S cm^{-1} for the AOC-xLiCl samples with $x=1$, 2, 3, 6, respectively. Since the low ionic conductivities of the crystalline phase of LiCl ($<10^{-7}$ S cm^{-1}) and $LiAlCl_4$ (2.1×10^{-5} S cm^{-1}),[10] it is supposed that the high ionic conductivity of the AOC-xLiCl samples should be attributed to the amorphous matrix with high lithium ion mobility. The obtained activation energies (Table S3) range from 0.487–0.636 eV, which are relatively higher than traditional halide SSEs while comparable to aluminum-based halides SSEs (such as $LiAlCl_4$, $NaAlCl_4$), which might be the character of these aluminum-contained SSEs. The influence of the thickness of the pellet and the applied pressure on the self-propagation reaction process and the ionic conductivities of synthesized AOC-2LiCl SSE is clarified in Figure S7. The high-resolution transmission electron microscopy (HRTEM) and corresponding fast Fourier transform (FFT) images (Figure S8) of typical AOC-2LiCl sample confirmed the highly amorphous states, with LiCl, $LiAlCl_4$ nanocrystallines (around 10 nm size) distribute inside the amorphous matrix. The amorphous contents determined by the Rietveld refinement Method[11] varied from 21–79.3 wt % with different x values (Table S2).

Nuclear magnetic resonance (NMR) analysis was further conducted on the AOC-xLiCl samples to explore the local structure. The ^{27}Al MAS NMR spectrum (Figure 2f) presents mainly three asymmetrically broadened peaks. The peak around 100 ppm should be assigned to $AlCl_4^-$.[12] The AOC-LiCl sample shows similar signal around 60–80 ppm compared to the synthesized AlOCl reference. Thus the intense NMR resonances at 75 ppm should be attributed to

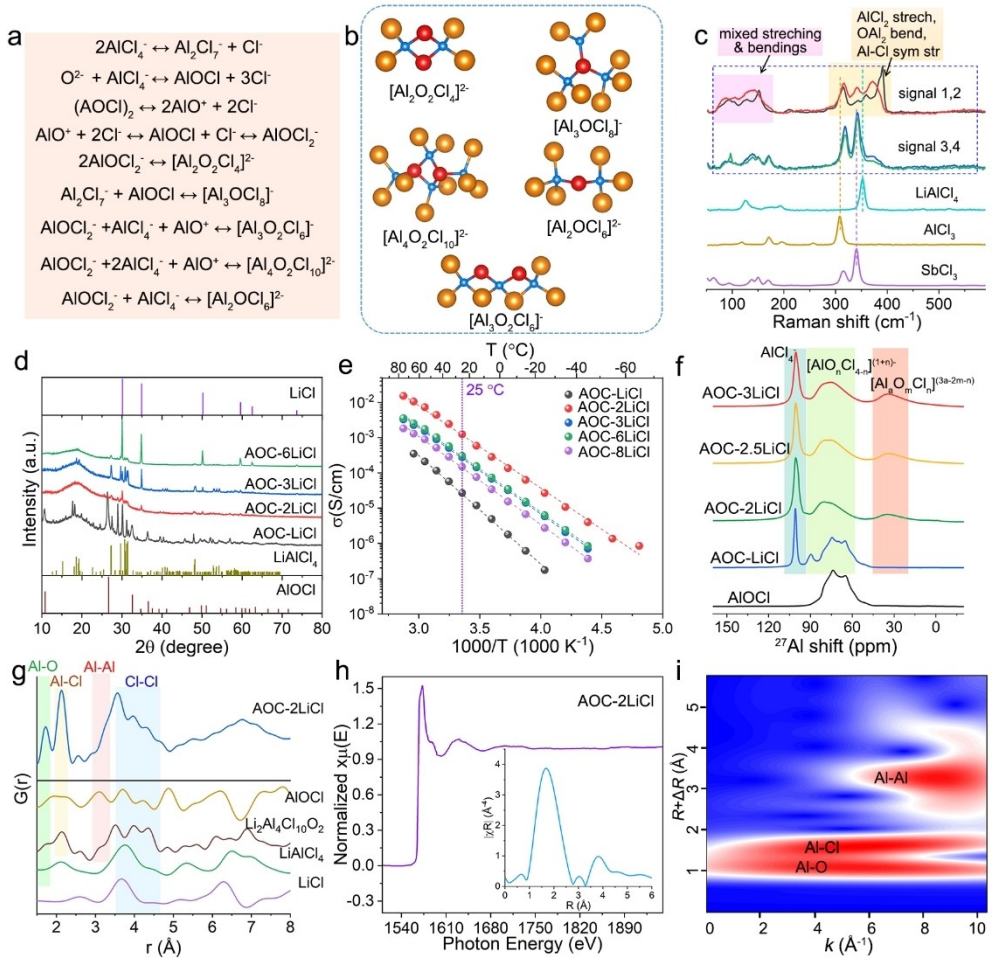

Figure 2. (a) Possible equilibriums might be achieved in the molten system during the self-propagating reaction. (b) Proposed models of oxidized chloroaluminate clusters based on calculated equilibrium states, the Al, O, and Cl atoms are shown in light blue, red, and orange, respectively. (c) Raman spectra of the self-propagating reaction from LiCl, $AlCl_3$, and Sb_2O_3 (molar ratio of 2 : 4.5 : 1). Different signals were recorded at different sites of the samples. Raman spectra of $LiAlCl_4$, $AlCl_3$, and $SbCl_3$ as references. (d) XRD patterns of the AOC-*x*LiCl ($x=1$, 2, 3, and 6) samples synthesized from LiCl, $AlCl_3$, and Sb_2O_3 (molar ratio of *x*: 4.5: 1). (e) Corresponding Arrhenius plots of the AOC-*x*LiCl samples. (f) ^{27}Al MAS NMR spectra of the AOC-*x*LiCl ($x=1$, 2, 3, and 6) samples. (g) PDFs of the AOC-2LiCl SSE. The calculated PDFs of $LiAlCl_4$, AlOCl, $Li_2Al_4Cl_{10}O_2$, and LiCl as references. Note that the structure of $Li_2Al_4Cl_{10}O_2$ is obtained by ionic substitution of $Ag_2Al_4Cl_{10}O_2$. (h) Al K-edge EXAFS spectroscopy of the AOC-2LiCl. (i) Wavelet transforms (WT) for the k^3-weighted Al K-edge EXAFS signals of the AOC-2LiCl.

the 4-coordinated Al species with different coordination species of $[AlO_nCl_{4-n}]^{(1+n)-}$. The NMR resonances at 34 ppm can be assigned to other oxidized chloroaluminate species ($[Al_aO_mCl_n]^{(3a-2m-n)}$) that are presented in Figure 2b. When $x \geq 2$, the ^{27}Al MAS NMR spectra of AOC-*x*LiCl are almost the same, indicating the similar local structural environments of aluminum species. Moreover, the NMR resonance assigned to $AlCl_4^-$ is independent of the $LiAlCl_4$ crystalline reflected by XRD pattern, demonstrating that the $AlCl_4^-$ species also exists in the amorphous matrix of the AOC-*x*LiCl samples.

Pair distribution function (PDF) analysis was performed to identify the unique local structures of AOC-2LiCl (Figure 2g). The PDF of AOC-2LiCl show peaks at 1.74 Å and 2.13 Å that could be attributed to Al–O and Al–Cl pairs in the first shell of the oxidized chloroaluminate species ($[Al_aO_mCl_n]^{(3a-2m-n)}$), respectively. The interatomic distances of Al–O and Al–Cl pairs in the first shell are almost identical in different $[Al_aO_mCl_n]^{(3a-2m-n)}$ clusters (Figure S9), giving the narrow peaks, while those of Al–Al and Cl–Cl vary with structures (Figure S10, 11), leading to a broaden peaks between 3–5 Å. But we still could identify the Al–Al pairs around 3 Å and the Cl–Cl pairs around 3.5 Å of multiple $[Al_aO_mCl_n]^{(3a-2m-n)}$ clusters.

Figure 2h presents the experimental extended X-ray absorption fine structure (EXAFS) results of AOC-2LiCl, demonstrating the nearest neighbor Al local environment. The Feff modeling fitting[13] in the k space for $k^3\chi(k)$ shows good agreement with the experimental data (Figure S12). The Fourier transform (FT) k^3-weighted $\chi(k)$ Al K-edge EXAFS spectrum of AOCl-2LiCl in the R space (insert in Figure 2h) shows the main peak at 1.7 Å which should be ascribed to the backscattering from O^{2-} and Cl^- coordination. This was further shown in the wavelet transformed

(WT)-EXAFS spectrum of Al K-edge in Figure 2i, which can not only give the distance information but also provide a straightforward view of the signal contributions (Al–O, Al–Cl, and Al–Al scatterings).[14] The Al–O, Al–Cl, and Al–Al scatterings in the WT-EXAFS spectrum prove the formation of $[Al_aO_mCl_n]^{(3a-2m-n)}$ clusters in the AOC-*x*LiCl SSEs, consistent with the PDF analysis results.

When further replacing LiCl into LiBr or LiI, the XRD patterns of the obtained samples with different molar ratios of LiBr or LiI, $AlCl_3$, and Sb_2O_3 (x:4.5:1, $1 \le x \le 3$) were shown in Figure 3a, b. When using LiBr as the lithium salt, like in the case of LiCl (Figure 2d), XRD patterns assigned to both $LiAlCl_4$ and AlOCl can be seen when $x=1$ (Figure 3a). While only $LiAlCl_4$ crystalline phase can be observed when $x \ge 2$. This was also confirmed by the high-resolution synchrotron-based XRD patterns (Figure S13). Considering the high boiling point of $SbBr_3$ (280 °C), $SbBr_3$ might not be fully removed during the heating process at 250 °C. XPS analysis was further conducted to determine the composition and proved that there's only a small amount of Br species (Br:Cl=1:55) in the final product, demonstrating that LiBr almost fully reacted with Sb_2O_3 (Figure S14). When using LiI as the lithium salt, except from the sample with low LiI salt content, almost all the XRD patterns can be assigned to crystalline SbI_3 phase ($x \ge 2$, Figure 3b). The existence of crystalline SbI_3 should be due to its highest boiling point (401.6 °C). It should be noted that, no matter what the crystalline phase is, high RT conductivities over 10^{-3} S cm^{-1} can still be achieved for AOC-2LiBr and AOC-2LiI SSEs when the molar ratio is 2:4.5:1 for lithium salt: $AlCl_3$: Sb_2O_3 (Figure 3c, d), even for the samples with high contents (~40 wt %, Table S2) of SbI_3 crystalline phase.

Combined with the conductivity behavior of AOC-*x*LiX samples, it is proposed that the amorphous components in

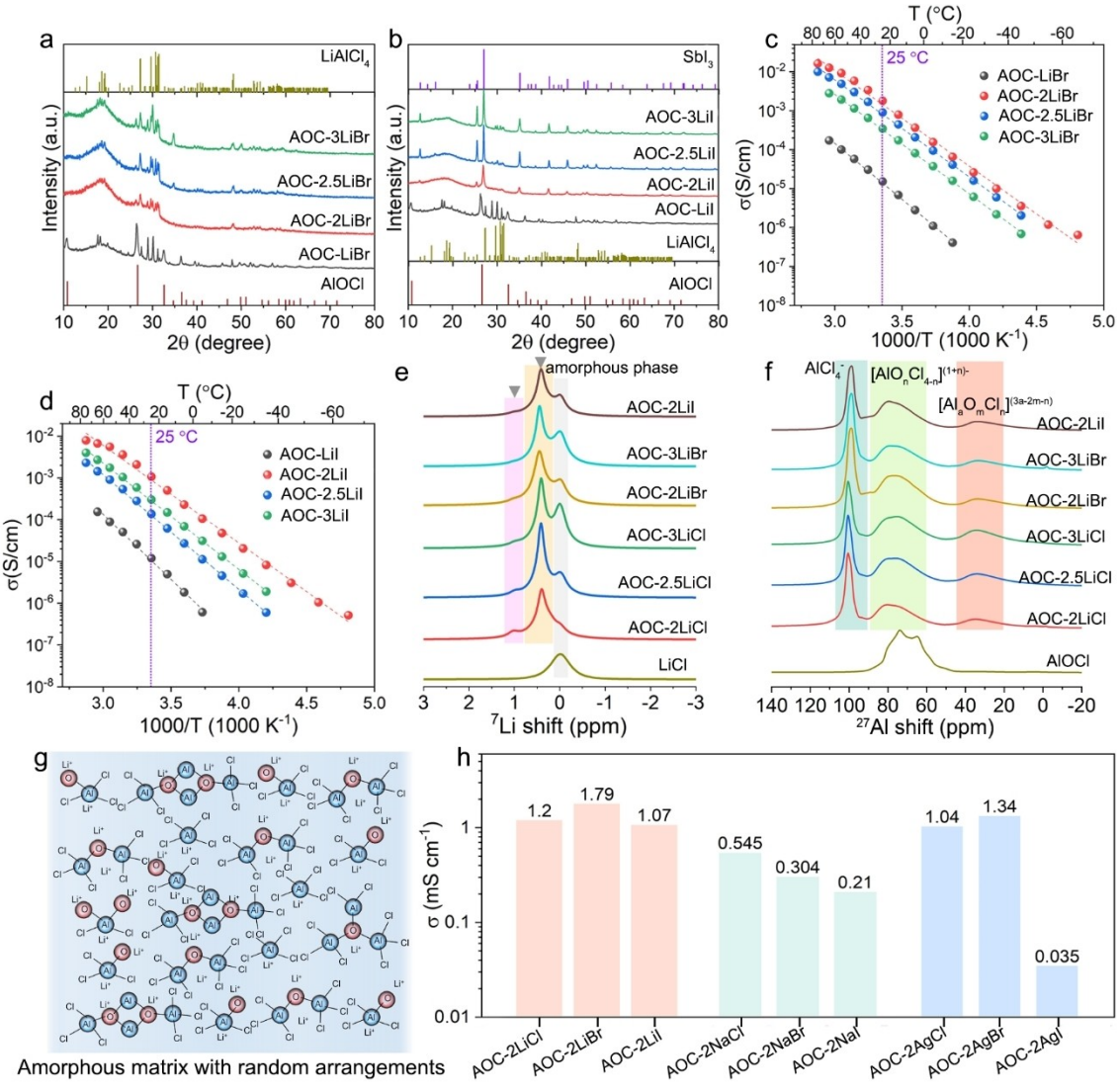

Figure 3. (a) XRD patterns of the AOC-*x*LiBr SSEs synthesized from LiBr, $AlCl_3$, and Sb_2O_3 (molar ratio of *x*: 4.5: 1). (b) XRD patterns of the AOC-*x*LiI SSEs synthesized from LiI, $AlCl_3$, and Sb_2O_3 (molar ratio of *x*: 4.5: 1). (c) Corresponding Arrhenius plots of the AOC-*x*LiBr SSEs. (d) Corresponding Arrhenius plots of the AOC-*x*LiI SSEs. (e) ^{7}Li NMR and (f) ^{27}Al NMR of the AOC-*x*LiX SSEs. (g) The schematics of the amorphous matrix in AOC-*x*LiCl SSEs. (h) RT ionic conductivities of the AOC-*x*LiX, AOC-*x*NaX, and AOC-*x*AgX SSEs.

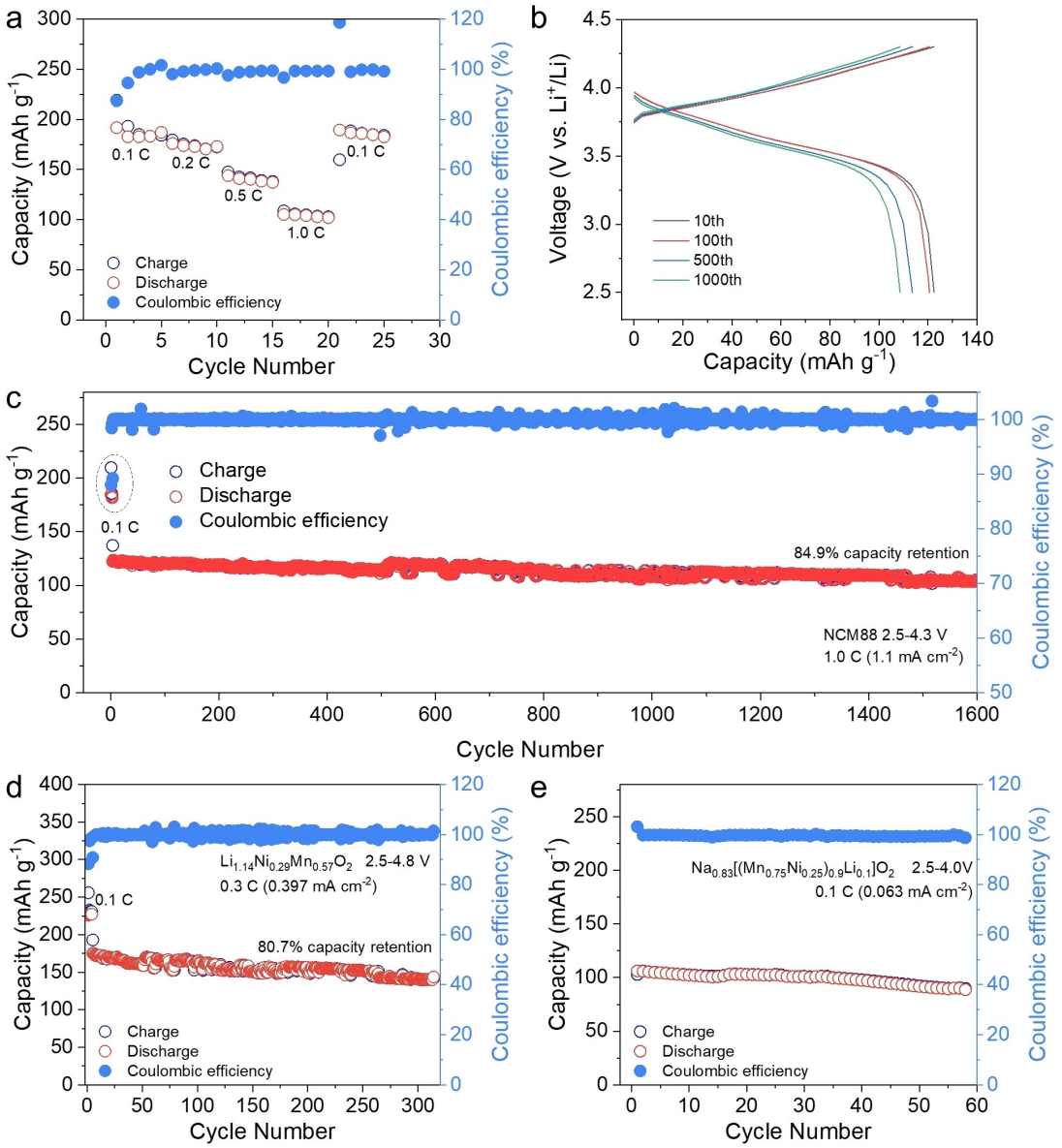

Figure 4. (a) Rate capability of NCM88 ASSB with AOC-2LiCl SSE. (b) Charge/discharge curves and (c) cycling stability of the NCM88 ASSB at 1 C (1.1 mA cm^{-2}) rate at 25 °C. (d) Cycling performance of the $Li_{1.14}Ni_{0.29}Mn_{0.57}O_2$ ASSB cycled between 2.5 and 4.8 V vs Li^+/Li at 0.3 C. (e) Cycling performance of the $Na_{0.83}[(Mn_{0.75}Ni_{0.25})_{0.9}Li_{0.1}]O_2$ all-solid-state sodium battery at 0.1 C at 25 °C.

these final products should play a key role in the super ionic conductivity. Two broad peaks around 0.45 ppm and 1.1 ppm were observed in the ^{7}Li MAS NMR spectra (Figure 3e) of all the AOC-*x*LiX SSEs, which are independent of the raw lithium salts, suggesting the same Li ions environment. Such broad peaks should be attributed to the newly formed amorphous matrix. Moreover, almost the same aluminum species can also be found for the AOC-*x*LiX SSEs as reflected by the ^{27}Al MAS NMR spectra in Figure 3f. Pair distribution function (PDF) analysis also indicates that comparable local environments of the amorphous components are present in these AOC-based materials. The PDF of AOC-2LiBr almost resembles that of AOC-2LiCl; as to AOC-2LiI, apart from peaks assigned to residual SbI_3, other peaks also are like AOC-2LiCl (Figure S15). It is obvious that the high ionic conductivity of these AOC-*x*LiX SSEs with different insulate nanocrystallines of LiCl, $LiAlCl_4$, SbI_3, etc. should be due to the introduction of a large fraction of highly amorphous matrix (Figure 3g) that providing fast diffusion pathways for the Li ions. Subsequent heating process at higher temperatures leads to the destruction of the conductive amorphous matrix and significantly decreased ionic conductivities (Figure S16). To further clarify the role of the amorphous matrix, we synthesized SSEs by replacing LiX into different salts, such as NaX and AgX (Figure S17–20). All the SSEs possess high RT ionic conductivities of 10^{-4}–10^{-3} S cm^{-1} (Figure 3e) regardless of the different crystalline phases. The high ionic conductivity might be due to the random configurations of these $AlCl_4^-$, $[AlO_nCl_{4-n}]^{(1+n)-}$, $[Al_2OCl_6]^{2-}$, $[Al_3OCl_8]^-$, and

$[Al_4O_2Cl_{10}]^{2-}$ species that creating numerous sites which enable smooth Li^+ (or other cations) migration pathways within the amorphous matrix.

The electrochemical stability window of the AOC-2LiCl SSE was measured (Figure S21) by linear sweep voltammetry (LSV), which indicates the high oxidative stability and compatibility with high-voltage cathode materials of the AOC-2LiCl SSE. To demonstrate the application of the material in ASSBs, commercial single-crystal $LiNi_{0.88}Co_{0.09}Mn_{0.03}O_2$ (NCM88) was used as the cathode, a dual-electrolyte construction was adopted, i.e., AOC-2LiCl with high oxidation stability as the catholyte and commercial Li_6PS_5Cl as the anolyte that directly contact with Li–In anode. The NCM88 ASSB exhibits good rate capability, as shown in Figure 4a. A high discharge capacity of 191.7 mAh g^{-1} is delivered at 0.1 C at 25 °C, with the initial Coulombic efficiency equal to 84.5 %. When the current density is increased to 1 C (200 mA g^{-1}), a high reversible capacity of 105 mAh g^{-1} is still provided. Meanwhile, excellent long-term cycling performance is shown in the NCM88 ASSB. Figure 4b compares the charge/discharge voltage profiles of selected cycles of the NCM88 ASSB at 1 C (1.1 mA cm^{-2}) between 2.5 and 4.3 V vs. Li^+/Li, showing minor cell polarization. After 1600 cycles, a discharge capacity of 103.9 mAh g^{-1} (84.9 % capacity retention), as well as the Coulombic efficiency of 99.95 %, is still delivered (Figure 4c), highlighting the superior stability of the AOC-2LiCl SSE matching both the NCM88 cathode and the sulfide solid electrolyte. The NCM88 ASSB with the AOC-3LiCl SSE also retained 80 % of its initial reversible capacity after 2000 cycles at 1 C (1.16 mA cm^{-2}) (Figure S22). More importantly, the ASSB with lithium-rich $Li_{1.14}Ni_{0.29}Mn_{0.57}O_2$ cathode delivers a high capacity of 175.3 mAh g^{-1} at 0.3 C (0.312 mA cm^{-2}) and maintains 80.7 % capacity retention over 300 cycles when cycled at 2.5–4.8 V vs. Li^+/Li (Figure 4d), demonstrating the high oxidation stability of the AOC-2LiCl SSE. Additionally, the application of AOC-2NaCl SSE in all-solid-state sodium batteries is also demonstrated. $Na_{0.83}[(Mn_{0.75}Ni_{0.25})_{0.9}Li_{0.1}]O_2$ | AOC-2NaCl | $Na_{2.9}PS_{3.9}Cl_{0.1}$ | Na–Sn cells show good cycle performance. As shown in Figure 4e and Figure S23, exhibiting an initial reversible capacity of 106.2 mAh g^{-1} at 0.1 C, the cell stably operated for over 60 cycles with a capacity retention of 83.5 % (Figure 4e). The electrochemical performance presented here proves both the high oxidation limit and the good compatibility with oxide cathodes of the aluminum-based oxychloride SSEs, indicating their promising application as catholytes in ASSBs.

Conclusion

In this study, we report a universal and facile self-propagating route for the synthesis of cost-effective aluminum-based oxyhalide SSEs. This versatile self-propagating approach allows for the synthesis of diverse aluminum-based oxyhalide SSEs (AOC-*x*MX, M = Li, Na, Ag, X = Cl, Br, I), leading to high ionic conductivities exceeding 10^{-3} S cm^{-1} at 25 °C for different cations (Li^+, Na^+, Ag^+). The crystalline and amorphous structures of AOC-xLiCl SSEs were decoupled by different techniques. XRD, Raman spectra, ^{27}Al MAS NMR analysis, PDF, and EXAFS analysis reveal the existence of LiCl and $LiAlCl_4$ in the crystalline phase while $AlCl_4^-$ and various oxidized chloroaluminate species ($[Al_aO_mCl_n]^{(3a-2m-n)}$) as the main species in the amorphous matrix. In the series of AOC-*x*LiX (X = Cl, Br, I) SSEs, it is proved that their similar fast Li^+ migration behavior is independent of the crystalline phase, which is evidenced by the AOC-*x*LiI ($x \geq 2$) samples which only show XRD peaks that assigned to SbI_3. Further using the examples of AOC-*x*NaX and AOC-*x*AgX SSEs, we demonstrate how the oxidized chloroaluminates with different configurations create various sites that enable fast and universal cations migration. Their high conductivities, low cost, high abundance, simple synthesis, and stability at high voltage make them attractive and promising for highly-needed proper catholyte in combination with high-voltage, high-energy-density cathodes such as $Li[Li_xNi_yMn_zCo_{1-x-y-z}]O_2$.

Supporting Information

The authors have cited additional references within the Supporting Information.[15]

Acknowledgements

This research was supported by the National Natural Science Foundation of China (No. 22379127), Ningbo Yongjiang Talent Introduction Programme (2023A-184-G), the Guangdong High-level Innovation Institute project (2021B0909050001), the China Postdoctoral Science Foundation (Number 2023M743354), the Natural Sciences and Engineering Research Council of Canada (NSERC), Canada Research Chair Program (CRC), Canada Foundation for Innovation (CFI), Ontario Research Fund, the University of Western Ontario, and Eastern Institute of Technology, Ningbo.

The authors thank beamline BL02B02 of the Shanghai Synchrotron Radiation Facility and the Brockhouse X-ray Diffraction and Scattering-High Energy Wiggler Beamline at the Canadian Light Source for providing the beamtime. The authors thank Prof. Gongming Wang and the Instruments Center for Physical Science of the University of Science and Technology of China for NMR measurements.

Conflict of Interest

The authors declare no conflict of interest.

Data Availability Statement

The data that support the findings of this study are available from the corresponding author upon reasonable request.

Keywords: self-propagating synthesis · oxyhalide solid electrolyte · solid-state electrolyte · superionic conductor · all-solid-state battery

[1] a) N. Kamaya, K. Homma, Y. Yamakawa, M. Hirayama, R. Kanno, M. Yonemura, T. Kamiyama, Y. Kato, S. Hama, K. Kawamoto, *Nat. Mater.* **2011**, *10*, 682–686; b) Y. Tanaka, K. Ueno, K. Mizuno, K. Takeuchi, T. Asano, A. Sakai, *Angew. Chem.* **2023**, *135*, e202217581.
[2] a) T. Asano, A. Sakai, S. Ouchi, M. Sakaida, A. Miyazaki, S. Hasegawa, *Adv. Mater.* **2018**, *30*, 1803075; b) X. Li, J. Liang, N. Chen, J. Luo, K. R. Adair, C. Wang, M. N. Banis, T. K. Sham, L. Zhang, S. Zhao, *Angew. Chem.* **2019**, *131*, 16579–16584; c) Y.-C. Yin, J.-T. Yang, J.-D. Luo, G.-X. Lu, Z. Huang, J.-P. Wang, P. Li, F. Li, Y.-C. Wu, T. Tian, *Nature* **2023**, *616*, 77–83; d) L. Hu, J. Wang, K. Wang, Z. Gu, Z. Xi, H. Li, F. Chen, Y. Wang, Z. Li, C. Ma, *Nat. Commun.* **2023**, *14*, 3807.
[3] a) H. Kwak, J.-S. Kim, D. Han, J. S. Kim, J. Park, G. Kwon, S.-M. Bak, U. Heo, C. Park, H.-W. Lee, *Nat. Commun.* **2023**, *14*, 2459; b) S. Yu, J. Noh, B. Kim, J.-H. Song, K. Oh, J. Yoo, S. Lee, S.-O. Park, W. Kim, B. Kang, *Science* **2023**, *382*, 573–579.
[4] L. Zhou, T.-T. Zuo, C. Y. Kwok, S. Y. Kim, A. Assoud, Q. Zhang, J. Janek, L. F. Nazar, *Nat. Energy* **2022**, *7*, 83–93.
[5] J. B. Wiley, R. B. Kaner, *Science* **1992**, *255*, 1093–1097.
[6] T. Dai, S. Wu, Y. Lu, Y. Yang, Y. Liu, C. Chang, X. Rong, R. Xiao, J. Zhao, Y. Liu, *Nat. Energy* **2023**, 1–8.
[7] R. W. Berg, H. A. Hjuler, N. J. Bjerrum, *Inorg. Chem.* **1984**, *23*, 557–565.
[8] a) K. Zachariassen, R. W. Berg, N. Bjerrum, J. H. Von Barner, *J. Electrochem. Soc.* **1987**, *134*, 1153; b) R. W. Berg, *Z. Naturforsch. A* **2007**, *62*, 157–168.
[9] R. Berg, T. Ostvold, *Acta chemica Scandinavica. Series A. Physical and inorganic chemistry* **1986**, *40*, 445–451.
[10] N. Tanibata, S. Takimoto, K. Nakano, H. Takeda, M. Nakayama, H. Sumi, *ACS Materials Lett.* **2020**, *2*, 880–886.
[11] K. Yasukawa, Y. Terashi, A. Nakayama, *J. Am. Ceram. Soc.* **1998**, *81*, 2978–2982.
[12] N. Tanibata, S. Takimoto, S. Aizu, H. Takeda, M. Nakayama, *J. Mater. Chem. A* **2022**, *10*, 20756–20760.
[13] B. Ravel, M. Newville, *J. Synchrotron Radiat.* **2005**, *12*, 537–541.
[14] a) H. Funke, A. Scheinost, M. Chukalina, *Phys. Rev. B* **2005**, *71*, 094110; b) H. Funke, M. Chukalina, A. C. Scheinost, *J. Synchrotron Radiat.* **2007**, *14*, 426–432.
[15] a) G. Ren, N. Zhang, X. Feng, H. Zhang, P. Yu, S. Zheng, D. Zhou, Z. Tian, X. Liu, *Chinese Physics B* **2020**, *29*, 016101; b) K. Yasukawa, Y. Terashi, A. Nakayama, *J. Am. Ceram. Soc.* **1998**, *81*, 2978–2982; c) A. Jain, S. P. Ong, G. Hautier, W. Chen, W. D. Richards, S. Dacek, S. Cholia, D. Gunter, D. Skinner, G. Ceder, *APL Mater.* **2013**, *1*.

Manuscript received: January 19, 2024
Accepted manuscript online: April 24, 2024
Version of record online: ■■, ■■

Research Articles

Solid-State Electrolytes

S. Zhang, Y. Xu, H. Wu, T. Pang, N. Zhang, C. Zhao, J. Yue, J. Fu, S. Xia, X. Zhu, G. Wang, H. Duan, B. Xiao, T. Mei, J. Liang,* X. Sun,* X. Li* **e202401373**

A Universal Self-Propagating Synthesis of Aluminum-Based Oxyhalide Solid-State Electrolytes

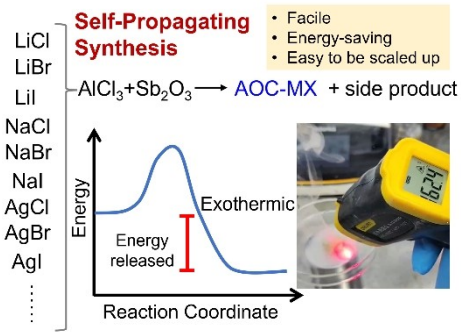

A facile strategy is developed to realize the scalable synthesis of cost-effective aluminum-based oxyhalide SSEs, which involves a self-propagating method by the exothermic reaction of the raw materials. This strategy enables the synthesis of various aluminum-based oxyhalide SSEs with tunable components and high ionic conductivities (over 10^{-3} S cm^{-1} at 25 °C) for different cations (Li^+, Na^+, Ag^+).